AAS 19-329

TRAJECTORY DESIGN USING QUASI-PERIODIC ORBITS IN THE MULTI-BODY PROBLEM

Brian P. McCarthy* **and Kathleen C. Howell†**

Incoporating quasi-periodic orbits (QPOs) into the preliminary design process offers a wider range of options to meet mission constraints and address the challenges in a complex trade space. In this investigation, QPO stability and alternative QPO family continuation schemes are examined to meet various types of trajectory constraints. Additionally, trajectory arcs from QPOs are exploited to generate transfers between periodic orbits. By leveraging the natural dynamical structures associated with QPOs, novel low cost transfers emerge.

INTRODUCTION

There has been a growing interest in the exploitation of libration point orbits in space exploration, in both robotic and human spaceflight. In 2010, ARTEMIS became the first mission to leverage the Earth-Moon L_1 and L_2 libration point orbits.[1] In 2015, the DSCOVR mission was launched into a quasi-periodic Lissajous orbit about the Sun-Earth L_1 point as the first deep space mission for NOAA.[2] NASA currently plans to launch the Orion spacecraft into a lunar Distant Retrograde Orbit (DRO) for Exploration Mission 1 (EM-1)[3] in 2019 and to utilize a southern L_2 Near Rectilinear Halo Orbit (NRHO) for the Gateway in the 2020s.[4] While both DROs and NRHOs are periodic in the circular restricted three-body problem (CR3BP) and periodic NRHOs are available in the bicircular four-body problem,[5] these orbits are quasi-periodic when transitioned to the ephemeris model. However, the CR3BP also offers an understanding of the fundamental characteristics for quasi-periodic behavior. Incorporating quasi-periodic orbits during preliminary design in the CR3BP leads to greater efficiency when transitioning to the ephemeris model.

All of the previous mission scenarios offer unique challenges associated with the trajectory design. First, EM-1 will test the Orion capsule, the first human-rated vehicle in deep space since the Apollo era. A 90-minute shadow constraint limits the duration that the Orion vehicle can spend in the shadow of another body. In this investigation, a lunar eclipse strategy is developed that exploits the natural dynamics of quasi-DROs to offset the shadow geometry. Second, the current baseline orbit for the Gateway is nearly stable and there are known challenges associated with transfer design to and from these orbits.[6,7] A strategy that leverages quasi-periodic motion to develop transfer trajectories between NRHOs, similar to those being used for the Gateway, is explored. Lastly, quasi-periodic orbits are locations of interest for both space telescopes and heliophysics missions; the quasi-periodic hyperbolic stable manifolds are integrated to construct direct transfers from the

*Ph.D. Student, School of Aeronautics and Astronautics, Purdue University, West Lafayette, IN 47907; mccart71@purdue.edu

†Hsu Lo Distinguished Professor of Aeronautics and Astronautics, School of Aeronautics and Astronautics, Purdue University, West Lafayette, IN 47907; howell@purdue.edu

Earth vicinity to quasi-periodic orbits. In general, quasi-periodic orbits provide alternative trajectory design strategies to meet a variety of mission constraints.

DYNAMICAL MODELS

The dynamical model for most of the preliminary designs in this investigation is the CR3BP. In the CR3BP, two gravitational bodies, P_1 and P_2, remain in circular, Keplerian orbits about their mutual barycenter or center of mass. A third body, i.e., a spacecraft, moves under the influence of the two gravitational bodies and is assumed to be massless. The model is defined relative to a rotating coordinate system, where the +$\hat{x}$-direction is defined from the barycenter to the second primary, P_2. The $\hat{z}$-direction is defined in the direction of orbital angular momentum for P_1 and P_2; the $\hat{y}$-direction completes the orthonormal triad. The position and velocity of P_3 relative to the barycenter in the rotating frame are defined $\vec{x} = \begin{bmatrix} x & y & z & \dot{x} & \dot{y} & \dot{z} \end{bmatrix}^T$, where the first three elements are the position components and the last three elements are the velocity components. A CR3BP system is characterized by a single nondimensional parameter, $\mu = m_2/(m_1 + m_2)$, where m_1 and m_2 are the masses of P_1 and P_2, respectively. There are five well known equilibrium solutions in the CR3BP, denoted L_i, where $i = 1, ..., 5$. The CR3BP admits a single integral of motion, the Jacobi Constant (JC). The Jacobi Constant is a function of the pseudo-potential and the velocity magnitude as determined relative to the rotating reference frame,

$$JC = 2U^* - v^2 \tag{1}$$

where $v = \sqrt{\dot{x}^2 + \dot{y}^2 + \dot{z}^2}$, or the velocity magnitude in the rotating frame. Note that U^* is the pseudo-potential, a function of the position of the third body relative to the center of mass in the rotating frame,

$$U^* = \frac{1}{2}(x^2 + y^2) + \frac{\mu}{r} + \frac{1-\mu}{d} \tag{2}$$

where $d = \sqrt{(x+\mu)^2 + y^2 + z^2}$ and $r = \sqrt{(x-1+\mu)^2 + y^2 + z^2}$, or the distance of the third massless body relative to P_1 and P_2, respectively. The Jacobi Constant is an energy-like quantity that characterizes motion in a CR3BP system. Thus, the Jacobi Constant defines the bounds for the motion in 3-dimensional space. In Equation (1), the v^2 term cannot be negative, so the motion is bounded by locations where $v^2 > 0$. These bounding surfaces are called the Zero-Velocity Surfaces (ZVS). One of the advantages of the CR3BP is that the system is time invariant since the motion of only the third body is reflected in the state vector. The CR3BP offers higher fidelity and additional behaviors in comparison to conics, but reduced complexity compared to the ephemeris model. Furthermore, trajectory characteristics generally persist when moving results in the CR3BP to the higher fidelity ephemeris model.

The ephemeris model offers a high fidelity gravity model by incorporating the ephemeris states of the planets included in the model. For this investigation, the ephemeris model includes the Sun, Earth, and Moon as point mass bodies. Examining trajectories transitioned to the ephemeris model validates the existence of geometries that represents the space environment for an actual mission scenario.

QUASI-PERIODIC ORBITS

Quasi-periodic orbits exist in the vicinity of periodic solutions in the CR3BP. The eigenvalues from the monodromy matrix associated with a periodic orbit determine the type of motion in the

vicinity of a periodic orbit. Complex eigenvalues of unit magnitude indicate the existence of a center subspace and indicate quasi-periodic motion in the vicinity of the orbit. In fact, an infinite number of quasi-periodic solutions exist in families of invariant tori in the vicinity of a periodic orbit. An invariant torus is defined by the number of number of fundamental frequencies, such that an n-dimensional torus possesses n fundamental frequencies that characterize the motion. Equilibrium solutions and periodic orbits in the CR3BP are examples of 0-dimensional and 1-dimensional tori, since the equilibrium solutions remain fixed and periodic orbits possess a single fundamental frequency associated with the period of the orbit. Quasi-periodic orbits exist on tori where two or more frequencies defined the motion, or $n > 1$. The current investigation builds upon the computation and applications of 2-dimensional tori. The two fundamental frequencies that define the motion for a 2-dimensional torus are termed the longitudinal and latitudinal frequencies. Consider a sample torus rendered in configuration space in Figure 1(a). The longitudinal frequency is represented by the motion of the blue circle, while the latitudinal frequency corresponds to the red circle, or the transverse motion around the surface. Subsequently, any location on the 2-dimensional torus is defined by two angles, θ_0 and θ_1. Various analytical approximations and numerical techniques are available to compute quasi-periodic orbits. Analytical and semi-analytical techniques using the Lindstedt-Poincaré method as well as center manifold reduction are computationally efficient, but limited effectiveness beyond the close proximity of the central periodic orbit.[8–10] Numerical techniques are computationally expensive, however, a wider range of solutions are accessible.[11–15] This investigation employs a method developed by Olikara and Howell,[16] and further generalized by Olikara and Scheeres.[13] This method employs a stroboscopic mapping technique to develop a discretized invariant circle or invariant curve for use in a differential corrections scheme. In the CR3BP, the time associated with the stroboscopic map, T_0, is defined by the period of the longitudinal frequency for a particular quasi-periodic orbit. The invariant curve is a representation of the 2-dimensional flow on a quasi-periodic orbit in the CR3BP. However, given that the full representation of flow cannot be propagated, individual trajectories are numerically integrated to discretize the flow. A simple representation of an invariant curve is then represented in Figure 1(b). A single trajectory segment, with the initial state located on the invariant curve is integrated for time T_0, where the trajectory path has a first return to the stroboscopic map. The integration time is the period associated with the longitudinal frequency, such that,

$$T_0 = \frac{2\pi}{\dot{\theta}_0} \tag{3}$$

where $\dot{\theta}_0$ is the longitudinal frequency. The state at the first return to the invariant curve on the stroboscopic map rotates by an angle, ρ, relative to the initial state on the invariant curve, defined,

$$\rho = \frac{2\pi\dot{\theta}_1}{\dot{\theta}_0} = T_0\dot{\theta}_1 \tag{4}$$

where $\dot{\theta}_1$ is the latitudinal frequency. For each return through the stroboscopic map, the state at each return rotates by ρ relative to the previous state. Subsequently, at the m^{th} return through the stroboscopic map, the initial state rotates by $m\rho$. Furthermore, if a single trajectory arc associated with a quasi-periodic orbit is propagated for $t \to \infty$, then the full invariant curve is represented on the stroboscopic map. Also note, if the rotation angle is a factor of 2π, then the frequency ratio is commensurate, resulting in a period orbit.

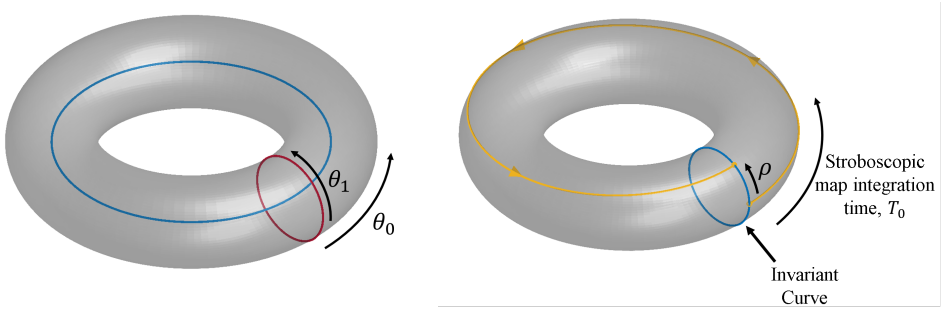

Figure 1. (a) Longitudinal and latitudinal frequency representation on 2-dimensional torus in configuration space. (b) A 2-dimensional torus with the invariant curve (blue), the rotation angle ρ, and a single trajectory (yellow) propagated to the first return to the invariant curve.

Computation

The invariant curve is constructed numerically given the fundamental periodic orbit and its characteristics including the period and stability properties. The invariant curve is discretized into N states, $\vec{u}_i(\theta_0, \theta_{1i})$, where $i = 1, 2, ..., N$ and N is number of discretized states representing the invariant curve, θ_0 is the longitudinal location, and θ_{1i} is the latitudinal location for the i^{th} discretized state on the invariant curve. An invariance constraint is formulated using the rotation angle, ρ,

$$\vec{u}_i(\theta_0, \theta_{1i}) - \mathbf{R}(-\rho)\vec{u}(\theta_0, \theta_{1i} + \rho) = \vec{0} \tag{5}$$

where $\mathbf{R}(-\rho)$ is the rotation operator that removes the rotation of the states around the invariant curve at the first return to the stroboscopic map. By enforcing the invariance constraint, 2-dimensional toroidal motion is ensured. A free variable and constraint differential corrections scheme is employed using the invariance constraint in Equation (5), in a single or multiple shooting formulation.[17] However, an initial guess is required to seed the differential corrections scheme, one that is reasonably accurate. First, the states representing the invariant curve are defined, i.e.,

$$\vec{u}_i^0(\theta_0, \theta_{1i}) = \epsilon \left(\mathrm{Re}[\vec{v}_C] \cos(\theta_{1i}) + \mathrm{Im}[\vec{v}_C] \sin(\theta_{1i}) \right) \tag{6}$$

where $\vec{u}_i^0(\theta_0, \theta_{1i})$ is the i^{th} state on the invariant curve associated with θ_{1i}, $\vec{v}_C$ is the eigenvector associated with the center mode of the underlying periodic orbit, and ϵ is a small quantity. The period of the fundamental orbit is employed as the initial guess for the integration time, T_0^0, or the longitudinal period. An initial guess for the rotation angle is generated using the angular location of the center subspace eigenvalue on the unit circle in the complex plane, i.e.,

$$\rho^0 = \tan^{-1}\left(\frac{\mathrm{Im}(\lambda_C)}{\mathrm{Re}(\lambda_C)} \right) \tag{7}$$

where λ_C is the eigenvalue associated with the center subspace. For a single shooting formulation, the elements of the free variable vector are comprised of the discretization states, ρ, and T_0. The elements of the constraint vector include the invariance constraint from Equation (5) and one selected parameter to maintain as fixed relative to the associated period orbit; this parameter typically possesses some physical significance and serves as the continuation parameter. To generate a family

of solutions, two phase constraints are also enforced to ensure uniqueness of each family member. In this investigation, Jacobi Constant, mapping time, and frequency ratio are examined as the fixed continuation parameters. Figure 2 illustrates a few members of the resulting three different families that originate from the same periodic vertical orbit. For constant energy families, as in Figure 2(a),

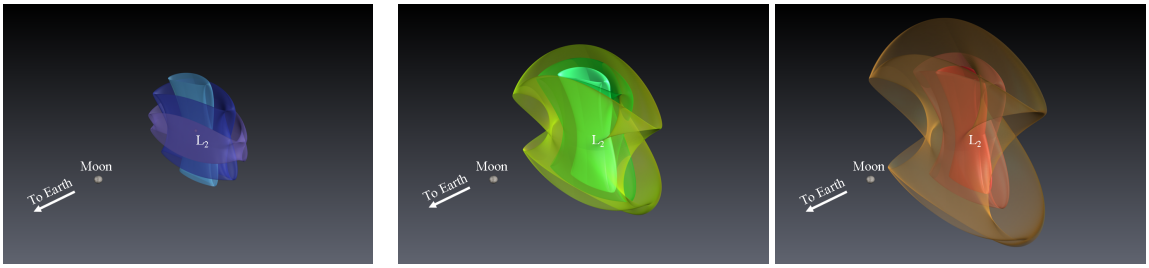

(a) (b) (c)

Figure 2. Given the same periodic vertical orbit: (a) Constant energy quasi-vertical family (b) Constant mapping time quasi-vertical family and (c) constant frequency ratio quasi-vertical family with the same underling periodic vertical orbit.

each member of the family possesses the same Jacobi Constant value as the underlying periodic orbit. Constant energy families are useful for designs that require accessing regions of space for the lowest cost, i.e., minimum energy change. Plotted in Figure 2(b), all members of a constant mapping time family share same longitudinal period which is equal to the period of the central periodic orbit. Eclipse avoidance is a focus for application of a constant mapping time family of orbits, specifically when the mapping time is in resonance with the eclipsing body. However, both constant energy and constant mapping time families encounter difficulties during numerical continuation when integer values in the fundamental frequency ratios are encountered, as noted by Bosanac.[18] When the fundamental frequencies are commensurate, the torus collapses to a period-M orbit, where M is the integer ratio, and the continuation scheme terminates. To avoid the difficulties associated with commensurate frequency ratios, a constant frequency ratio family is also generated. The frequency ratio is defined as a function of only the rotation angle, ρ, for 2-dimensional tori,

$$\frac{\dot{\theta}_0}{\dot{\theta}_1} = \frac{2\pi}{\rho} \tag{8}$$

Subsequently, constant frequency ratio families are also termed constant rotation angle families. By initializing a constant frequency ratio family from a periodic orbit that does not occur near a period multiplying bifurcation, integer frequency ratios are not encountered during continuation. Quasi-periodic orbit families are not limited to the these three types, this characterization is appropriate for the applications in this investigation.

QUASI-PERIODIC ORBIT STABILITY

Assessing the stability of orbits in the CR3BP supplies information on motion in the vicinity of that orbit and aid in exposing new types of solutions. Stability properties associated with quasi-periodic orbits are explored via the differential of the variations relative to the tori identified on the stroboscopic map. In particular, rather than assessing a fixed point, deviations from the invariant curve are examined. Additionally, due to the reduceability of the CR3BP, a metric defined as a

stability index is characterized for quasi-periodic orbits. For unstable quasi-periodic orbits, hyperbolic stable and unstable invariant manifolds exist that asymptotically approach and depart the torus corresponding to the given quasi-periodic orbit. Olikara and Scheeres previously examined stability as well as hyperbolic manifolds for quasi-periodic orbits in the CR3BP; Baresi and Scheeres examined stability associated with quasi-periodic orbits in the vicinity of small bodies.[13,19] Recall that the invariance constraint ensures that the states used to discretize an invariant curve are equal to the states at the first return to the map, after removing the rotation by the angle ρ around the invariant curve. The partial derivative of the invariance condition with respect to the state variations yields a differential of the discretized invariant curve on the stroboscopic map, i.e.,

$$\mathbf{DG} = \tilde{\mathbf{\Phi}}(\mathbf{R}(-\rho) \otimes \mathbf{I}) \tag{9}$$

where $\mathbf{R}(-\rho)$ is the rotation operator, $\mathbf{I}$ is a 6×6 identity matrix, $\otimes$ is the Kronecker product operator, and $\tilde{\mathbf{\Phi}}$ a block diagonal matrix comprised of STMs. The STMs are all propagated from the initial time to the first return to the stroboscopic map. The resulting dense matrix, $\mathbf{DG}$, of dimension $6N \times 6N$, represents the differential of the variations for the discretized invariant curve. The eigenstructure of $\mathbf{DG}$ provides information on the stability of the quasi-periodic orbit. As Jorba notes, tori in the CR3BP are reduceable.[20] Consequently, the eigenvalues of the $\mathbf{DG}$ are related to the eigenvalues of the Floquet matrix through the relationship

$$\vec{\lambda} = \Lambda_r e^{-\mathrm{i}\vec{k}\rho} \tag{10}$$

where ρ is the rotation angle defined in Equation (4), Λ_r is the r^{th} eigenvalue of the Floquet matrix, where $r = 1, 2, ..., 6$, and $\vec{\lambda}$ is a vector of eigenvalues associated with the r^{th} eigenvalue of the Floquet matrix, and $\vec{k}$ is defined,

$$\vec{k} = \begin{cases} \begin{bmatrix} -\frac{N-1}{2} & \dots & -1 & 0 & 1 & \dots & \frac{N-1}{2} \end{bmatrix} & \text{if } N \text{ is odd} \\ \begin{bmatrix} -\frac{N}{2} & \dots & -1 & 0 & 1 & \dots & \frac{N}{2} \end{bmatrix} & \text{if } N \text{ is even} \end{cases} \tag{11}$$

Consider an L_2 quasi-halo orbit in the Earth-Moon system, rendered in Figure 3. The eigenstructure of the quasi-halo orbit is plotted on the complex plane in Figure 3(b). As illustrated in the figure, the eigenvalues exist on concentric circles about the origin in the complex plane. A circle with a radius greater than 1 is associated with the unstable mode of the torus, while a circle with a radius less than 1 reflects the stable mode. Furthermore, the stable mode radius is the reciprocal of the unstable mode radius since eigenvalues in the Floquet matrix exist in reciprocal pairs for a Hamiltonian system.[21] Given the concentric circle structure for the eigenvalues, a stability index, ν, is defined such that,

$$\nu = \frac{1}{2}(R_u + \frac{1}{R_u}) \tag{12}$$

where R_u is the radius of the circle associated with the unstable mode. Quasi-periodic orbits that possess a stability index equal to 1 are considered stable, while stability indices greater than 1 indicate that the orbit is unstable. The stability index for the unstable quasi-halo orbit rendered in Figure 3(a) is $\nu = 1.3837$. The stability index over the family of constant energy quasi-halo orbits ($JC = 3.1389$) is plotted as a function of mapping time in Figure 4. The stability index characterizes the stability of a quasi-periodic orbit in a single, convenient metric. Stable and unstable quasi-periodic orbits are easily identified and the stability evolution for a family is represented as a single curve.

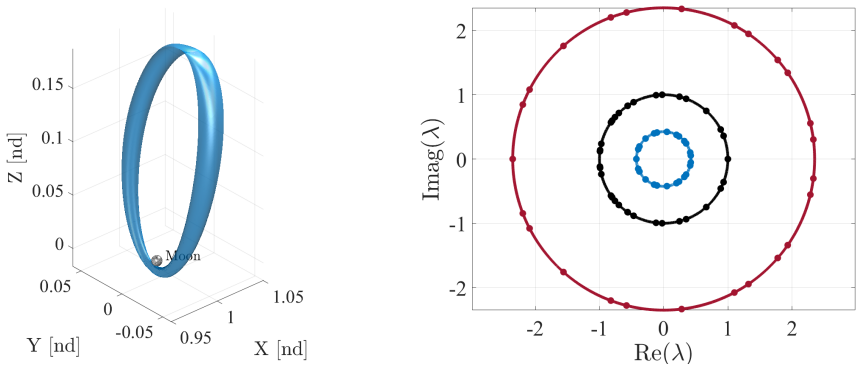

Figure 3. (a) Earth-Moon L_2 quasi-halo orbit ($JC = 3.044$) (b) Eigenstructure of DG matrix corresponding to the quasi-halo orbit computed with $N = 25$.

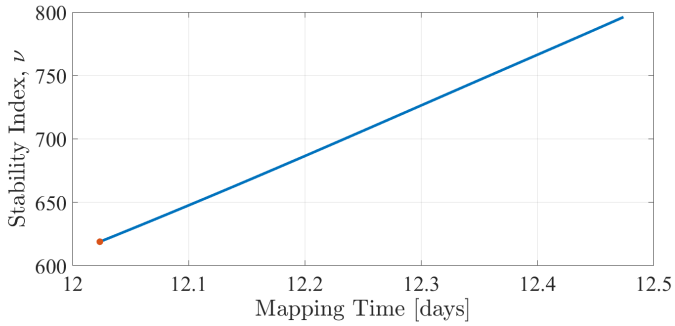

Figure 4. Stability index as a function of mapping time for an Earth-Moon L_1 constant energy quasi-halo family ($JC = 3.1389$). The red point represents the stability index of the periodic halo orbit associated with this quasi-halo orbit family.

Hyperbolic Manifolds

Hyperbolic invariant manifolds exist for quasi-periodic orbits that are considered unstable. The stable and unstable hyperbolic manifolds asymptotically approach and depart the torus, respectively. To compute stable/unstable manifolds, the eigenvectors associated with the stable and unstable eigenvalues of the **DG** matrix are exploited. Selecting the real stable/unstable eigenvalue ensures that the associated eigenvector also has no imaginary components. Consider the real stable and unstable eigenvalue, $\lambda_{s,r}$ and $\lambda_{u,r}$, respectively, from the **DG** matrix. The stable and unstable eigenvectors associated with the purely real stable and unstable eigenvalues are denoted $\vec{v}_{s,r}$ and $\vec{v}_{u,r}$, respectively. The eigenvectors are defined with $6N$ elements, corresponding to the N discretized states that represent the invariant curve. The elements of the eigenvectors are subdivided, such that

$$\vec{v}_{s,r} = \begin{bmatrix} \vec{v}_{1,s,r} \\ \vec{v}_{2,s,r} \\ \vdots \\ \vec{v}_{N,s,r} \end{bmatrix}, \vec{v}_{u,r} = \begin{bmatrix} \vec{v}_{1,u,r} \\ \vec{v}_{2,u,r} \\ \vdots \\ \vec{v}_{N,u,r} \end{bmatrix}, \tag{13}$$

where $\vec{v}_{i,s,r}$ and $\vec{v}_{i,u,r}$ correspond to the 6-element stable and unstable directions, respectively, for the i^{th} state on the invariant curve. Subsequently, the states along the invariant curve are perturbed by a small value ϵ in the stable/unstable directions and integrated backwards/forwards to generate the global stable/unstable manifolds

$$\vec{x}_{i,s} = \vec{x}_i + \epsilon \frac{\vec{v}_{i,s,r}}{|\vec{v}_{i,s,r}|} \tag{14}$$

$$\vec{x}_{i,u} = \vec{x}_i + \epsilon \frac{\vec{v}_{i,u,r}}{|\vec{v}_{i,u,r}|} \tag{15}$$

where $\vec{x}_{i,s}$ and $\vec{x}_{i,u}$ represent the 6-dimensional stable and unstable initial state, respectively, of the i^{th} state on the invariant curve in non-dimensional barycentered coordinates, $\vec{x}_i$ represents the i^{th} state on the invariant curve with non-dimensional barycentered coordinates. However, Equations (14) and (15) only provide the initial states at a single longitudinal location. The STM is used to obtain the stable and unstable directions for states at other longitudinal locations along a torus. The projection of a torus in configuration space for an unstable quasi-halo orbit appears in Figure 5 along with snapshots at various times as the unstable manifold trajectory states evolve upon departure from the quasi-periodic orbit. The torus projection of the unstable manifold, as viewed in configuration

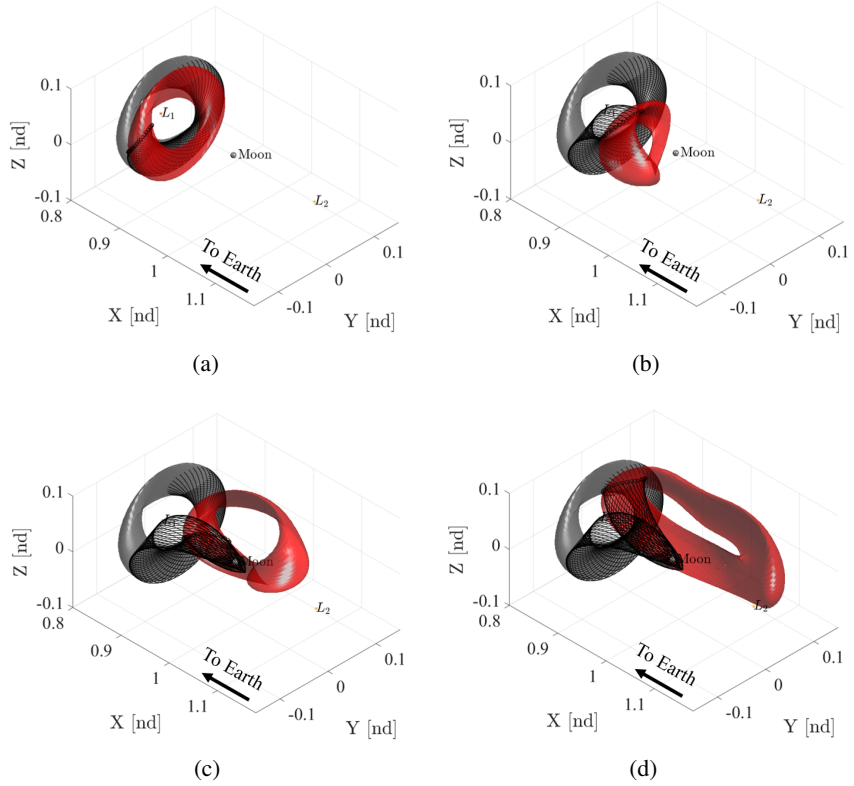

Figure 5. Unstable manifold in the +x-direction for an Earth-Moon L_1 quasi-halo orbit ($JC = 3.1389$). Trajectories associated with one invariant curve are plotted in black. A snap shot of the points comprising the manifold, in red, are recorded after (a) 7.79 days, (b) 9.75 days, (c) 11.39 days and (d) 13.02 days.

space, morphs as it is propagated forward in time towards the Moon. Similarly, the projection of the other unstable half-manifold in the direction of the Earth is rendered in Figure 6.

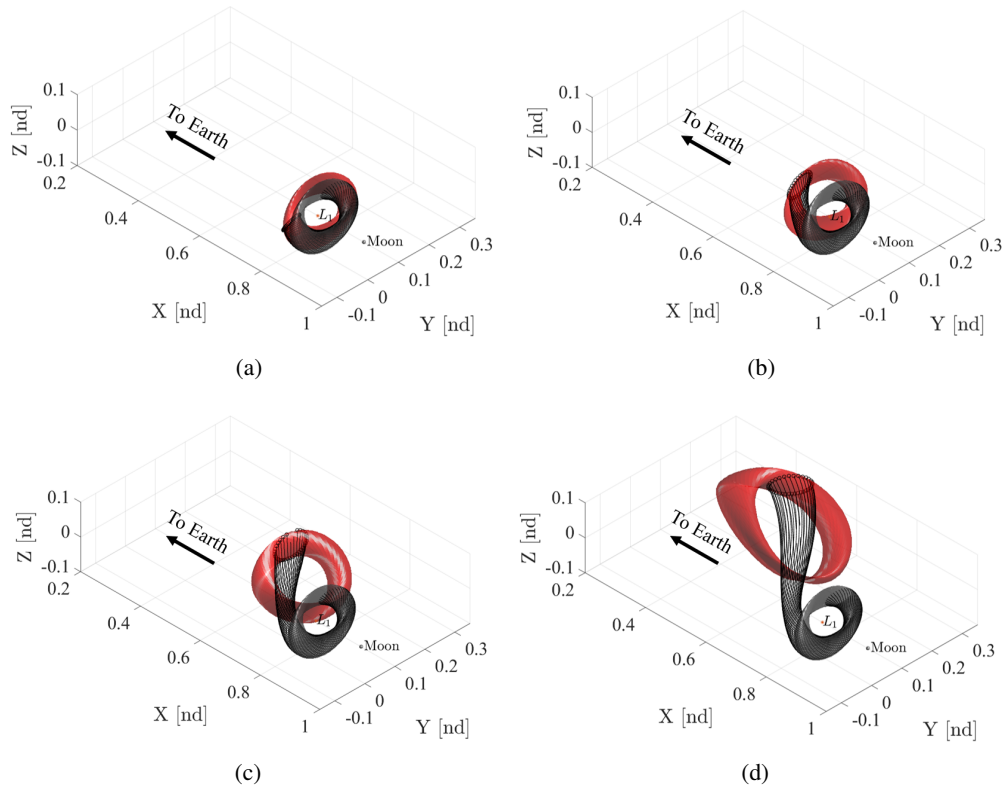

Figure 6. Unstable manifold in the -x-direction for an Earth-Moon L_1 quasi-halo orbit ($JC = 3.1389$). Trajectories associated with one invariant curve are shown in black. A snap shot of the points comprising the manifold, in red, are recorded after (a) 7.79 days, (b) 9.75 days, (c) 11.39 days and (d) 13.02 days.

ECLIPSE AVOIDANCE IN AN EARTH-MOON DRO

While numerous constraints drive a particular design, the impact of eclipsing influences many mission scenarios and nearly all mission concepts in cislunar space. For an operational orbit, eclipse avoidance is a common driver for trajectory design contraints, as many spacecraft rely on solar exposure to meet thermal and power requirements. These requirements subsequently limit the time interval during which a spacecraft is allowed to remain within the shadow of an occulting body. In the EM-1 mission plan, eclipse avoidance is an important aspect of the trajectory design due to the 90 minute maximum eclipse duration constraint for Orion.[3] Additionally, the target $70,000$ km DRO is planar in the Earth-Moon rotating frame, causing a disruption in the line of sight with the Earth when the trajectory passes behind the far side of the Moon.

To mitigate potential eclipsing in the Earth-Moon system while maintaining a constant line of sight with Earth, a synodic resonance is leveraged. A p:q synodic resonance is defined such that p periods of the spacecraft orbit are completed for every q synodic periods of the Moon, where the synodic period of the Moon is approximately 29.5 days. The Sun, Earth, and Moon geometry repeats over a synodic period of the Moon, T_{syn}, as illustrated in Figure 7. The repeatable geometry of the Moon relative to the Sun leads to repeatable eclipsing geometry as well. As a consequence, a 2:1 lunar synodic resonant DRO possesses a period equal to half of the synodic period of the Moon, or approximately 14.75 days. Since the Moon is a major occulting body, exploiting a syn-

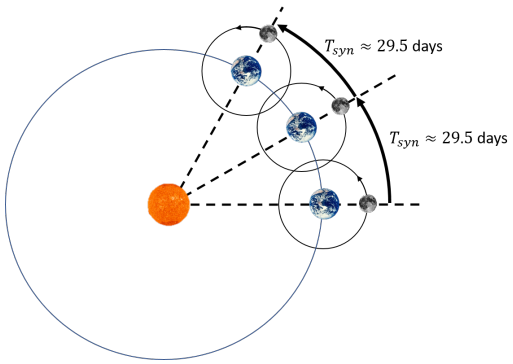

Figure 7. Sun-Earth-Moon geometry over two lunar synodic periods

odic resonance ensures the repeatability of the trajectory path with respect to the Moon location relative to the Sun. The family of constant mapping time quasi-DROs associated with the 2:1 lunar synodic resonant periodic DRO is computed, introducing an out of plane component. The constant mapping time is selected to preserve the resonance in terms of the mapping time in the quasi-DRO family relative to the 2:1 resonant planar, periodic DRO, plotted in Figure 8(a). All members of the quasi-DRO constant mapping family are stable, as the stability index is equal to 1 across the family. The planar, periodic 2:1 resonant DRO in green in Figure 8(a) and 8(b). One member of the associated constant mapping time family is plotted in configuration space as the grey transparent surface in Figure 8(b). The Sun-spacecraft line of sight disruption for the planar periodic DRO is approximately 2.3 hours for every revolution of the orbit. A quasi-DRO from the constant mapping time family is identified such that the $\hat{z}$-component in the Earth-Moon rotating frame allows for unobstructed line of sight with the Earth. On the invariant curve (black), a insertion location (red) is selected at a location of $\theta_1 = 0°$ such that a constant line of sight with Earth is achieved after 10 returns through the stroboscopic map. To visualize lunar eclipsing, CR3BP trajectories are viewed

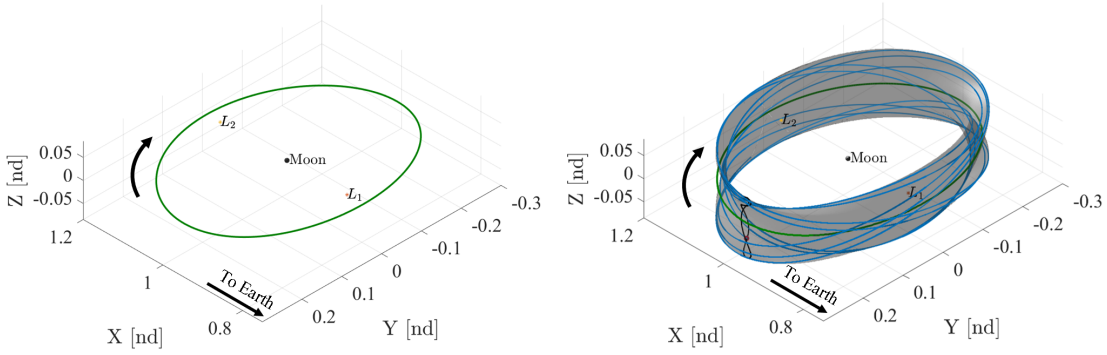

Figure 8. (a) Periodic 2:1 lunar synodic resonant DRO. (b) Quasi-DRO with a mapping time of 14.75 days (grey) and the associated planar periodic DRO (green). A trajectory segment (blue) is propagated for 10 returns through the stroboscopic map, or 147.5 days, where the red circle indicates the beginning of the trajectory. The initial invariant curve is plotted in black.

in the Sun-Moon rotating frame. The JPL DE421 ephemerides were used to obtain state information

of Sun, Earth and Moon in the ephemeris model.[22] When viewed in the Sun-Moon rotating frame, the lunar shadow is fixed and an eclisping event is evident when the path passes through the lunar shadow. Distinct gaps exist resonant quasi-DRO trajectory when viewed in this frame. If phased properly, a spacecraft avoids the lunar shadow without the use of eclipse avoidance maneuvers. The phasing is adjusted by inserting at different locations on the invariant curve. Figure 9 depicts two trajectories, plotted in Sun-Moon rotating frame; both trajectories are initiated with an initial epoch of June 1, 2020. The trajectory in Figure 9(a) has an insertion angle $\theta_1 = 0^\circ$ and encounters a lunar eclipse, plotted as the red arc in Figure 9(a) and the $\hat{y}\hat{z}$-projection in Figure 9(b). However, if the latitudinal insertion angle is changed to $\theta_1 = 80^\circ$, lunar eclipses are avoided. The quasi-DRO trajectory with no eclipsing events is plotted in Figure 9(c), with a $\hat{y}\hat{z}$-projection in Figure 9(d) illustrating that the trajectory does not pass behind the dark side of the Moon. The grey box in Figures 9(a) and 9(c) depicts the depth of the projections in Figures 9(b) and 9(d). Controlling the insertion location along the invariant curve allows a designer to adjust the phasing of the quasi-DRO to avoid lunar eclipse events.

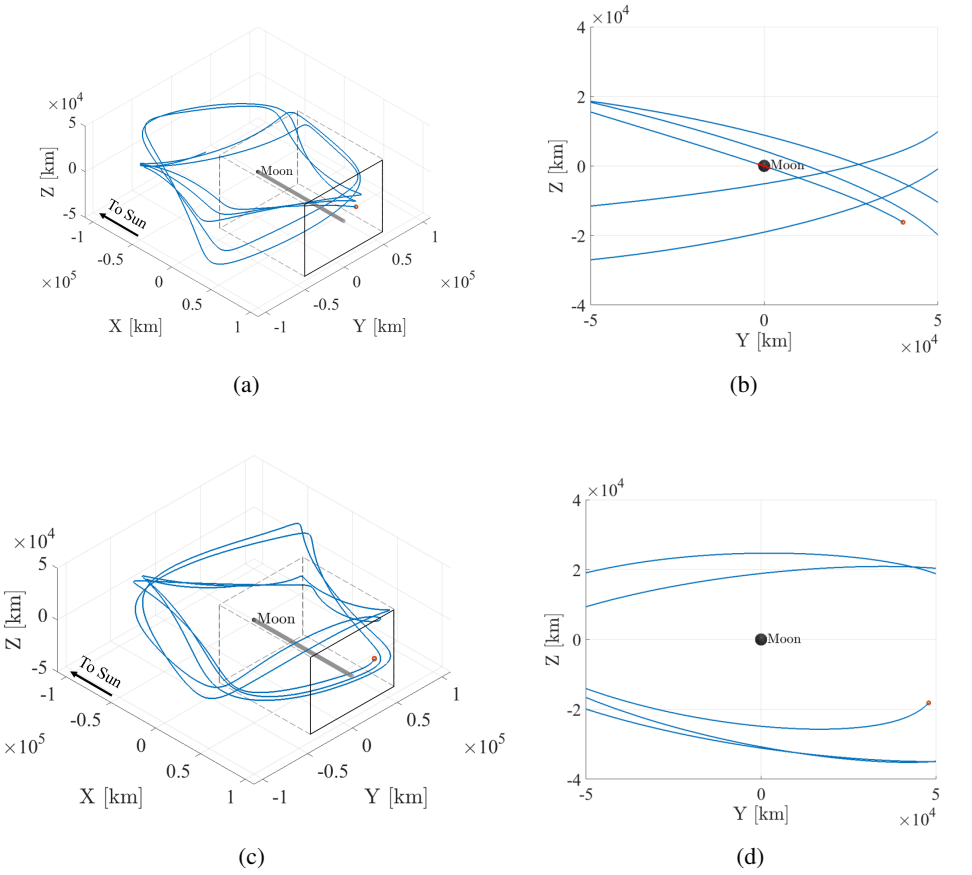

Figure 9. Quasi-DRO with eclipsing event (red) in the Sun-Moon rotating frame with an latitudinal insertion angle of $\theta_1 = 0^\circ$ in (a) 3-dimensional view and (b) the $\hat{y}\hat{z}$-view looking toward the Sun from the dark side of the Moon. The grey box shows the depth of the $\hat{y}\hat{z}$ projection. Using an latitudinal angle of $\theta_1 = 80^\circ$, eclipses are avoided, as plotted in (b) and (c).

Now consider the scenario where the insertion location along the invariant curve is fixed, but the

insertion epoch is varied. A quasi-DRO trajectory arc is plotted in Figure 10(a) in the Sun-Moon rotating frame with an initial insertion epoch of June 1, 2020 and a latitudinal insertion location of $\theta_1 = 0°$. Again, an eclipsing event occurs, plotted in red, when the path passes through the lunar shadow. The $\hat{y}\hat{z}$-projection of the trajectory, rendered in Figure 10(b), shows the red arc of the trajectory experience an eclipsing event as it passes behind the Moon. By changing the insertion epoch to June 15, 2020, and fixing the insertion location on the invariant curve to $\theta_1 = 0°$, the lunar shadow passes through a gap in quasi-DRO trajectory, as plotted in Figure 10(c), avoiding eclipsing events for the duration of the simulation. A $\hat{y}\hat{z}$-projection of the trajectory in the Sun-Moon rotating frame is plotted Figure 10(d), showing that the trajectory does not pass through the dark side of the Moon. Finally, to ensure the geometry persists in the higher fidelity model, the quasi-DRO trajectory with a initial epoch of June 15, 2020 and a latitudinal insertion angle of $\theta_1 = 0°$ is converged in the Sun-Earth-Moon ephemeris model using differential corrections. The ephemeris trajectory is rendered in Figure 11 viewed in the Sun-Moon rotating frame. By choosing the insertion epoch and the insertion location on the invariant circle such that the lunar shadow passes through gaps in the trajectory, lunar eclipse avoidance is achieved for long term duration in the quasi-DRO.

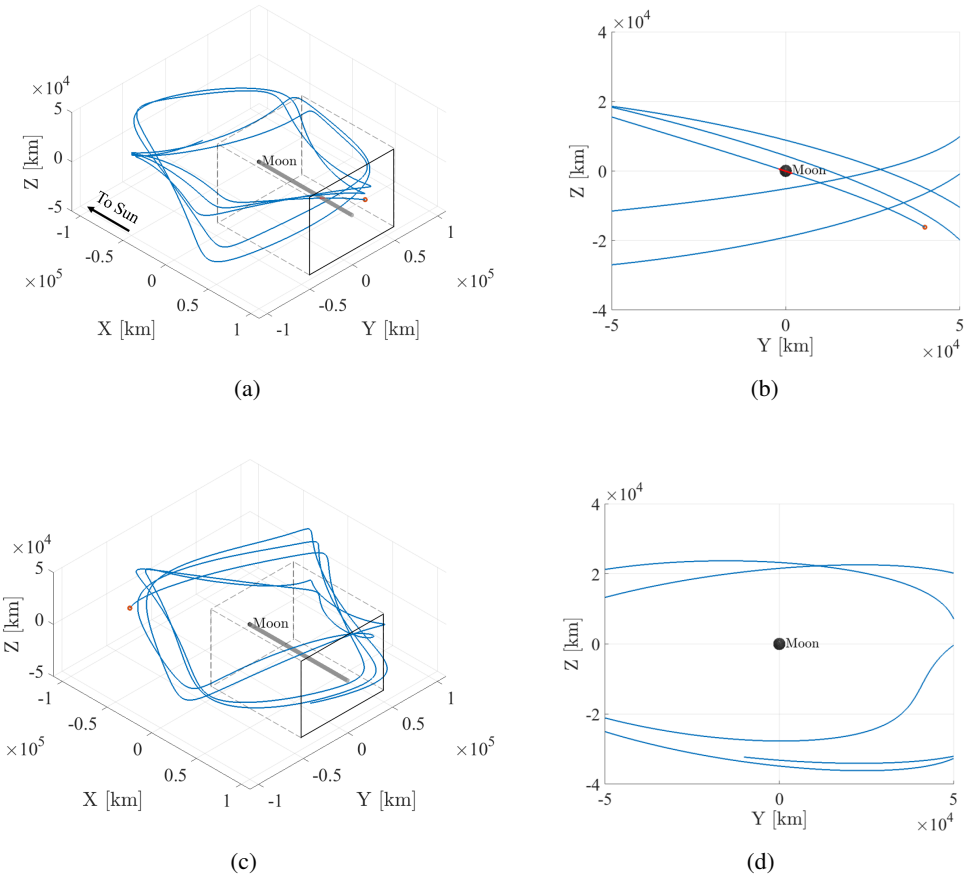

Figure 10. Quasi-DRO with eclipsing event (red) in the Sun-Moon rotating frame with an insertion epoch of June 1, 2020 in (a) 3-dimensional view and (b) the $\hat{y}\hat{z}$-view looking toward the Sun from the dark side of the Moon. The grey box shows the depth of the $\hat{y}\hat{z}$ projection. Using an insertion epoch of June 15, 2020, eclipses are avoided, as plotted in (b) and (c).

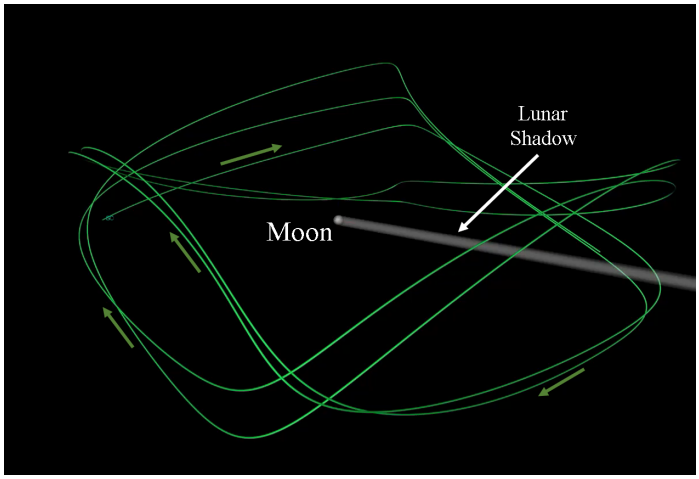

Figure 11. Quasi-DRO trajectory converged in the Sun-Earth-Moon ephemeris model as viewed in the Sun-Moon rotating frame.

TRANSFER TRAJECTORY DESIGN IN THE EARTH-MOON SYSTEM

Any transfer between periodic orbits requires that the periodic orbits intersect one another, or that a transfer path intersects both the originating and destination orbits in position space. Maneuvers adjust the energy to achieve desired destination orbit or transfer trajectory characteristics. In a conic model, various numerical and analytical methods are available to compute transfer trajectories that minimize time of flight, required energy, or maneuver magnitude.[23] However, in regimes where multiple bodies significantly influence the path of the spacecraft, the dynamics are more complex, necessitating new techniques to compute transfer trajectoies. Moreover, there are no known analytical solutions for periodic orbits in multi-body regimes. Various strategies are effective to compute transfer trajectories between periodic orbits in multi-body regimes, however, incorporating quasi-periodic trajectory arcs into transfer trajectories between periodic orbits has not yet been widely explored.[7,24–31] Consider two periodic orbits in the Earth-Moon system, plotted in Figure 12(a). The originating orbit, in blue, is an unstable northern L_2 halo orbit and the destination orbit is a planar L_2 Lyapunov orbit. Introduce an L_2 quasi-halo orbit in the vicinity of both periodic orbits. A trajectory arc from the quasi-periodic orbit offers a good initial guess for a corrections scheme that converges on a continuous solution. With departure and arrival maneuvers on the periodic orbits, and allowing the location of the departure and arrival locations to vary, a transfer trajectory is computed in Figure 12(b). Exploiting a trajectory arc along the quasi-periodic provides a significant plane change that is required to arrive on the Lyapunov orbit. The maneuvers are modeled as impulsive for all examples. The departure $\Delta V_1 = 139.4$ m/s and the arrival $\Delta V_2 = 4.0$ m/s, for a total $\Delta V_{tot} = 143.4$ m/s. The time of flight required to complete the transfer is 186.9 days, where most of the time is spent approaching the $\hat{x}\hat{y}$-plane to minimize the $\hat{z}$-component of velocity. The example demonstrates that trajectory arcs from quasi-periodic orbits serve as successful initial guesses for transfers between periodic orbits. The ARTEMIS transfer trajectory design exploited a similar plane change technique using a quasi-periodic orbit[1]

The next step in the human spaceflight program is the Gateway program.[4] Plans for the lunar Gateway facility is operation in an L_2 NRHO that exists in a regime where the gravitational influence of the Earth cannot be neglected. Capabilities are required for excursions from the NRHO (near

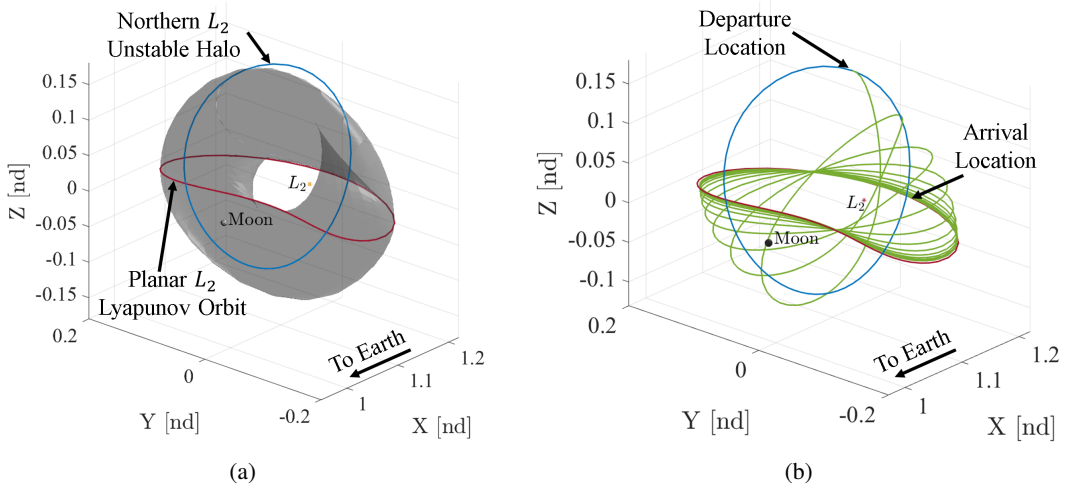

Figure 12. (a) Originating unstable halo orbit (blue), quasi-halo orbit torus used for a transfer initial guess (grey), and the destination planar Lyapunov orbit. (b) Converged transfer from an unstable halo orbit to a planar Lyapunov orbit in the Earth-Moon system.

the Moon) to other halo orbits (near the Earth-Moon L_2 libration point). Difficulties are known to exist in generating transfers between stable and nearly stable periodic orbits;[6,7] these transfer strategies add additional complexity. Quasi-periodic trajectories offer alternatives for transfers between nearly stable periodic NRHOs, similar to those considered for the lunar Gateway.[32,33] Consider two northern L_2 NRHOs in the Earth-Moon system with lunar periapsis radii of $r_p = 4,800$ km (blue) and $r_p = 12,610$ km (red), plotted in Figure 13. Both of these orbits are nearly stable and the stability indices are 1.5425 and 1.1762 for the departure and destination NRHOs, respectively. Also, consider a quasi-NRHO from constant frequency ratio family, whose fundamental periodic orbit has a lunar periapsis $r_p = 8,065$ km and a $\frac{\dot{\theta}_0}{\dot{\theta}_1} = 5.0305$. The quasi-periodic orbit is rendered as a grey surface in Figure 13. Both periodic NRHOs intersect the quasi-NRHO surface at multiple points and by selecting a quasi-periodic arc that is near the intersection points with both periodic orbits on the torus, an initial guess is generated. The light blue circles on the departure NRHO identify two locations where the periodic orbit intersects the quasi-NRHO surface. By allowing maneuvers at the departure and arrival locations and allowing the time of flight to vary, transfer trajectories are computed for both departure locations in Figure 13. The converged solution for departure location 1 is plotted in Figure 14(a). The departure maneuver $\Delta V_1 = 48.3$ m/s and the arrival maneuver $\Delta V_2 = 32.2$ m/s, for a total $\Delta V_{tot} = 80.5$ m/s. The converged transfer trajectory is plotted in green with a time of flight of 23 days. The transfer trajectory associated with departure location 2 is rendered in Figure 14(b). The transfer for departure location 2 occurs over a significantly shorter time of flight, 12.4 days, however the total maneuver cost is higher. For departure location 2, the $\Delta V_{tot} = 86.6$ m/s, where $\Delta V_1 = 51.3$ m/s and $\Delta V_2 = 35.3$ m/s.

A similar transfer strategy is also leveraged for transfers between synodic resonant NRHOs. The current baseline for the lunar Gateway is a 9:2 lunar synodic resonant southern L_2 NRHO ($r_p = 3,200$ km). Additionally, a 4:1 lunar synodic resonant southern L_2 NRHO ($r_p = 5,700$ km) delivers favorable eclipse avoidance properties.[33] A constant frequency ratio quasi-NRHO is computed from a periodic NRHO with a lunar periapsis radius of $r_p = 4,680$ km. A single quasi-NRHO from the

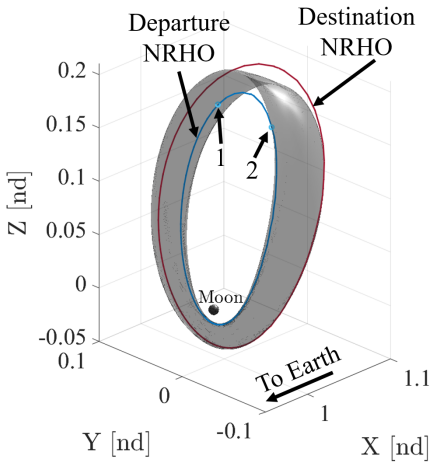

Figure 13. Departure (blue) and destination (red) NRHOs, with two potential departure locations (light blue) that intersect the torus projection (grey).

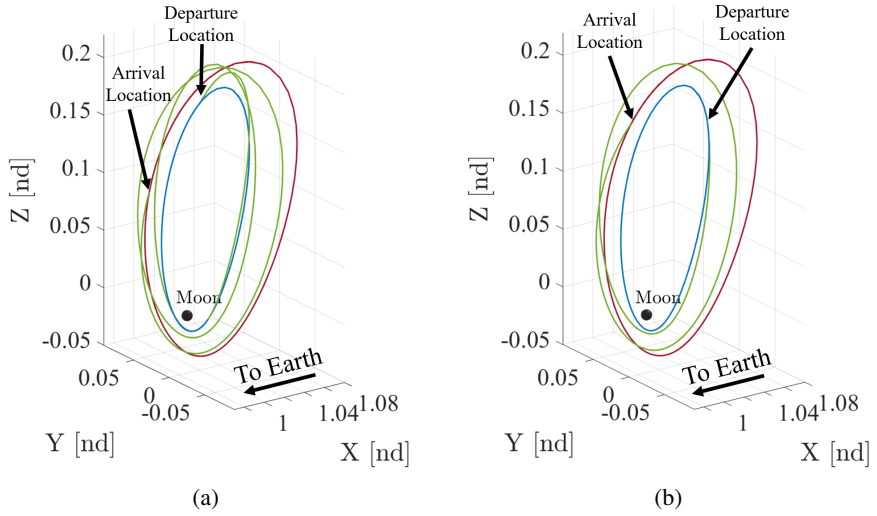

Figure 14. Converged transfer trajectories for (a) departure location 1 and (b) departure location 2.

family is selected such that the 9:2 and 4:1 resonant periodic NRHOs intersect the quasi-NRHO torus in configuration space, as depicted in Figure 15(a). At an intersection location along the 9:2 synodic resonant NRHO, a trajectory arc is propagated on the quasi-NRHO until it reaches the vicinity of the 4:1 synodic resonant NRHO. A differential corrections scheme permits impulsive departure and arrival maneuvers, converging on the solution rendered in Figure 15(b). The departure $\Delta V_1 = 25.6$ m/s and the arrival $\Delta V_2 = 24.0$ m/s, for a total $\Delta V_{tot} = 49.6$ m/s. The time of flight for the 9:2 to 4:1 synodic resonant NRHO is 11.4 days. Lunar synodic resonant NRHOs possess useful eclipse avoidance properties and quasi-NRHOs offer trajectory arcs for applications as transfer initial guesses.

The NRHO transfers in Fiqures 14 and 15 serve as feasible solutions in the CR3BP; the transfers

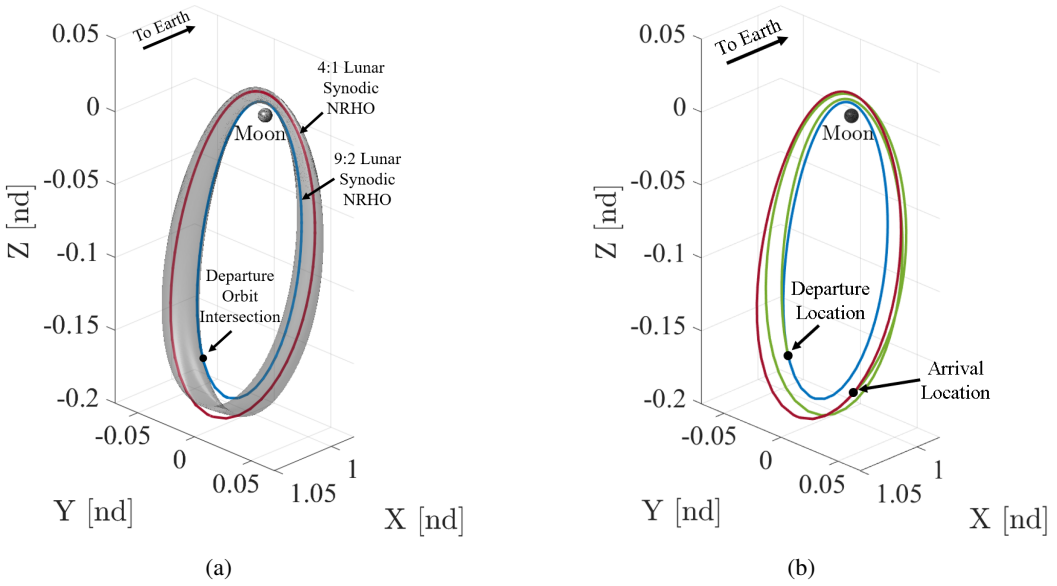

Figure 15. (a) Quasi-NRHO leveraged for transfer initial guess with departure orbit (blue) and arrival orbit (red). (b) Converged transfer trajectory (green) departing from a 9:2 lunar synodic resonant southern L_2 NRHO (blue) to a 4:1 lunar synodic resonant southern L_2 NRHO (red)

are not initially optimized. However, a theoretical minimum ΔV is computed to assess the feasible transfers in comparison to some theoretical minimum. Recall the Jacobi Constant as a function of the pseudo-potential and the velocity magnitude from Equation (1). To accommodate only the energy difference between the departure and arrival orbits, a theoretical minimum ΔV is constructed. Rearrange the Jacobi Constant equation to solve for velocity magnitude by simply computing the different between the departure velocity and the arrival velocity,

$$\Delta V_{min} = \sqrt{2U^* - JC_2} - \sqrt{2U^* - JC1} \tag{16}$$

where JC_2 is the desired Jacobi Constant, JC_1 is the Jacobi Constant corresponding to the departure location, and U^* is the pseudo-potential function from Equation (2). The pseudo-potential is evaluated at the departure location, since the equation provides the minimum maneuver magnitude to change to energy at that departure location. The resulting ΔV_{min} is the minimum velocity change required to achieve a Jacobi Constant of JC_2 at the departure location. From Equation (16), the theoretical minimum energy change is computed for each of the NRHO transfers and displayed in Table 1. Maneuver costs associated with feasible transfer solutions are not necessarily locally optimal minimum ΔV solutions. Using an optimization algorithm that employs an SQP routine, locally optimal ΔV solutions are also computed. Table 2 summarizes the local optimal total ΔV costs for each transfer. Note that the theoretical minimum maneuver costs are different than the same computation for the feasible solutions since the departure location is allowed to shift within the optimization routine. Optimal solutions that are near the theoretical minimum indicate that the maneuver directions that are nearly tangential. In summary, trajectory arcs from quasi-periodic orbits offer feasible NRHO transfer solutions with ΔV results near the theoretical minimum values and local optimal solutions further reduced total maneuver costs.

Table 1. Feasible transfer ΔV and theoretical minimum ΔV at the locally optimal departure location

Transfer	Theoretical Minimum ΔV (m/s)	Feasible Transfer ΔV (m/s)
Location 1	50.41	80.5
Location 2	51.19	86.6
9:2 to 4:1 NRHO	34.23	49.6

Table 2. Local optimal ΔV and theoretical minimum ΔV at the locally optimal departure location

Transfer	Theoretical Minimum ΔV (m/s)	Optimal Transfer ΔV (m/s)
Location 1	21.2	41.6
Location 2	31.4	71.5
9:2 to 4:1 NRHO	20.5	34.5

HYPERBOLIC MANIFOLDS FOR P_2 ACCESS IN THE SUN-EARTH SYSTEM

Unstable quasi-periodic orbits imply associated stable and unstable hyperbolic manifolds that define flow that asymptotically approaches and departs the unstable quasi-periodic orbit, respectively. Stable and unstable manifolds also supply transfer options in the vicinity of P_2 without deterministic maneuvers to insert or depart a quasi-periodic orbit, respectively. Some quasi-periodic orbits in the vicinity of L_1 and L_2 in various systems possess stable and unstable manifolds that pass in close proximity to the second primary. Consequently, hyperbolic manifolds deliver unique design alternatives in the vicinity of P_2.

Sun-Earth Lissajous Orbit Access from Earth

The Sun-Earth L_1 libration point is proven as a useful location for operations in support of solar observatory missions in recent years. Currently, NASA's ACE, WIND, and SOHO as well as NOAA's DSCOVR spacecraft reside in quasi-periodic orbits in the vicinity of the Sun-Earth L_1 libration point.[2,34] Additionally, the James Webb Space Telescope plans to operate in a quasi-periodic orbit near the Sun-Earth L_2 point in the early 2020s[35] and the WFIRST mission is scheduled to launch in 2026 to an libration point orbit in the same region.[36] Minimizing propellant costs aids in maximizing the science payload on the spacecraft and enabling missions that might otherwise not be possible, so efficient transfer trajectories serve as one approach for increasing efficiency and expanding options. Consider a Lissajous orbit in the vicinity of the Sun-Earth L_1 point in the CR3BP with a $\hat{z}$-amplitude of 940,000 km and a $\hat{y}$-amplitude of 660,000 km. By perturbing 3,500 states along the Lissajous orbit and propagating each state in reverse time, a time history for the trajectories representing the global stable half-manifold is computed. A minimum periapsis radius relative to Earth is recorded for a each trajectory arc and a heat map is created with the results appearing in Figure 16. The horizontal axis in Figure 16 is the longitudinal location, θ_0, for the initial condition on the torus and the vertical axis identifies the latitudinal location, θ_1. The color on the heat map corresponds to the minimum periapsis radius encountered along the propagated path, where warmer colors indicate higher periapsis radii and cooler colors indicate lower periapsis radii.

Selecting a point on the map with a periapsis radius relative to Earth near a Low Earth Orbit (LEO) perigee value yields a stable manifold trajectory that serves as an initial guess for a final transfer from the desired LEO perigee radius. The red circle on the heat map in Figure 16 corresponds to a periapsis radius of approximately 7,033 km. However, a perigee radius of 6,563 km matches the radius of a 185 km altitude LEO parking orbit. A differential corrections scheme is employed that constrains a 185 km altitude perigee at the Earth and ensures the trajectory is on the manifold approaching the quasi-vertical orbit. Using this corrections scheme, the parking orbit departure maneuver to insert onto the stable manifold is the only deterministic maneuver required in the model. The final converged trajectory is rendered in Figure 17; note that the transfer delivers the large out-of-plane component. Quasi-periodic stable manifolds yield transfer trajectory options from the close vicinity of P_2 to the quasi-periodic orbit in the CR3BP, where no deterministic maneuver is required to insert.

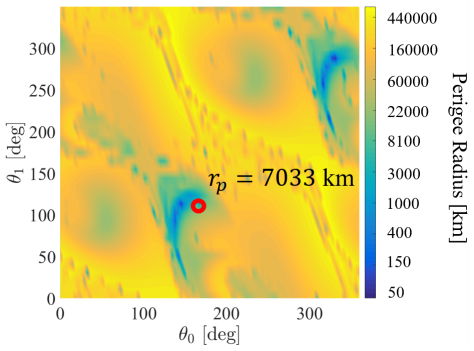

Figure 16. Periapsis heat map

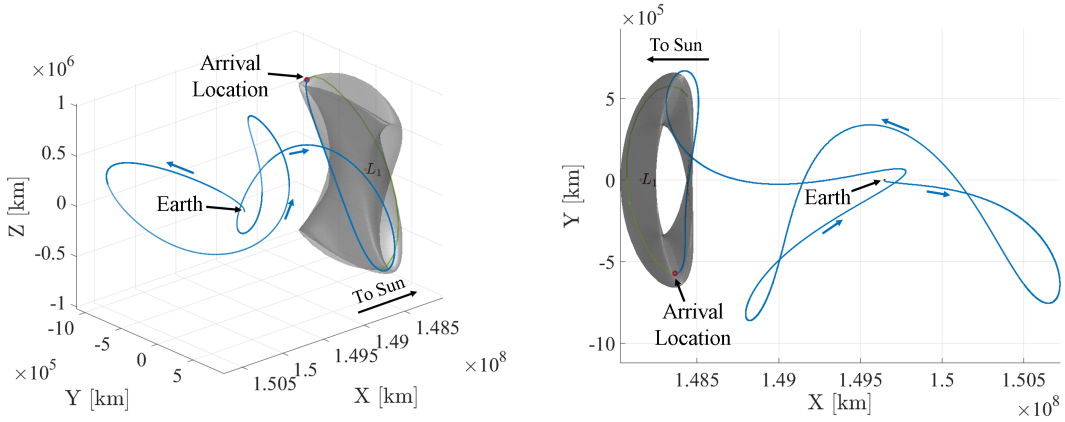

(a) (b)

Figure 17. (a) 3D view and (b) $\hat{x}\hat{y}$ projection of a transfer from LEO to quasi-periodic Sun-Earth L_1 Lissajous orbit.

SUMMARY

This investigation seeks to explore and develop useful techniques to leverage quasi-periodic orbits for trajectory design applications in multi-body environments. Three types of quasi-periodic families are discussed, each with specific advantages. Challenges are identified with the construction of constant energy and constant mapping time quasi-periodic orbits families through continuation. When integer ratios of fundamental frequencies are encountered, the numerical challenges are mitigated by modifying the continuation parameter to a constant frequency ratio. Stability of quasi-periodic orbits are characterized with a single stability metric and the hyperbolic manifolds are then computed. Three specific applications that employ quasi-periodic orbits in trajectory design illustrate the concept. First, lunar eclipse avoidance strategies are developed employing lunar synodic resonant quasi-DROs and the results are validated in a high-fidelity ephemeris model. The

use of quasi-periodic trajectory arcs as initial guesses for transfers between periodic orbits is also demonstrated. A trajectory arc from a quasi-halo orbit provides a significant plane change for a transfer from an unstable periodic halo orbit to a planar Lyapunov orbit. Quasi-NRHO trajectory arcs are leveraged to generate feasible transfers between nearly stable periodic NRHOs that deliver a transfer near the theoretical minimum energy change ΔV. Finally, the stable manifolds associated with a L_2 quasi-vertical orbit in the Sun-Earth system are exploited to determine a transfer trajectory from the Earth vicinity to the quasi-vertical orbit and a non-intuitive transfer trajectory is computed using periapsis heat maps.

ACKNOWLEDGEMENTS

The authors would like to thank the Purdue University School of Aeronautics and Astronautics, as well as the Rune and Barbara Eliasen Visualization Laboratory for facilities and financial support. The authors would also like to thank the Purdue Multi-Body Dynamics Research Group, specifically Andrew Cox, for insightful discussions about quasi-periodic orbits.

REFERENCES

[1] D. C. Folta, M. Woodard, K. Howell, C. Patterson, and W. Schlei, "Applications of Multi-Body Dynamical Environments: The ARTEMIS Transfer Trajectory Design," *Acta Astronautica*, Vol. 73, 2012, pp. 237–249.

[2] C. Roberts, S. Case, J. Reagoso, and C. Webster, "Early Mission Maneuver Operations for the Deep Space Climate Observatory Sun-Earth L1 Libration Point Mission," *AAS/AIAA Astrodynamics Specialist Conference*, Vail, Colorado, Aug. 2015.

[3] T. F. Dawn, J. P. Gutkowski, A. L. Batcha, S. M. Pedrotty, and J. Williams, "Trajectory Design Considerations for Exploration Mission 1," *AIAA Science and Technology Forum*, Kissimmee, Florida, Jan. 2018.

[4] K. Hambleton, "Deep Space Gateway to Open Opportunities for Distant Destinations," *web*, Mar. 2017. https://www.nasa.gov/feature/deep-space-gateway-to-open-opportunities-for-distant-destinations.

[5] D. Davis, K. Boudad, S. Phillips, and K. C. Howell, "Disposal, Deployment, and Debris in Near Rectilinear Halo Orbits," *29th AAS/AIAA Space Flight Mechanics Meeting*, Ka'anapali, Hawaii, Jan. 2019.

[6] E. M. Zimovan, K. C. Howell, and D. C. Davis, "Near Rectilinear Halo Orbits and Their Application in Cis-Lunar Space," *3rd International Academy of Astronautics Conference on Dynamics and Control of Space Systems*, Moscow, Russia, June 2017.

[7] L. Capdevila, D. Guzzetti, and K. C. Howell, "Various Transfer Options from Earth into Distant Retrograde Orbits in the Vicinity of the Moon," *AAS/AIAA Space Flight Mechanics Meeting*, Santa Fe, New Mexico, Jan. 2014.

[8] G. Gómez, J. Masdemont, and C. Simó, "Quasihalo Orbits Associated with Libration Points," *Journal of the Astronautical Sciences*, Vol. 46, Mar. 1999, pp. 135–176.

[9] R. W. Farquhar and A. A. Kamel, "Quasi-Periodic Orbits About the Translunar Libration Point," *Celestial Mechanics*, Vol. 7, June 1973, pp. 458–473.

[10] A. Jorba and J. Masdemont, "Dynamics in the Center Manifold of the Collinear Points of the Restricted Three Body Problem," *Physica D: Nonlinear Phenomena*, Vol. 132, July 1999, pp. 189–213.

[11] K. C. Howell and H. J. Pernicka, "Numerical Determination of Lissajous Trajectories in the Circular Restricted Three-Body Problem," *Celestial Mechanics*, Vol. 41, No. 1-4, 1988, pp. 107–124.

[12] G. Gomez and J. M. Mondelo, "The Dynamics Around the Collinear Equilibrium Points of the RTBP," *Physica D: Nonlinear Phenomena*, Vol. 157, Oct. 2001, pp. 283–321.

[13] Z. P. Olikara and D. J. Scheeres, "Numerical Methods for Computing Quasi-Periodic Orbits and Their Stability in the Circular Restricted Three-Body Problem," *IAA Conference on Dynamics and Control of Space Systems*, Porto, Portugal, Mar. 2012.

[14] E. Kolemen, N. J. Kasdin, and P. Gurfil, "Multiple Poincar Sections Method for Finding the Quasiperiodic Orbits of the Restricted Three Body Problem," *Celestial Mechanics and Dynamical Astronomy*, Vol. 112, Jan. 2012, pp. 47–74.

[15] F. Schilder, H. M. Osinga, and W. Vogt, "Continuation of Quasi-periodic Invariant Tori," *SIAM Journal on Applied Dynamical Systems*, Vol. 4, No. 3, 2005, pp. 459–488.

[16] Z. Olikara and K. C. Howell, "Computation of Quasi-Periodic Invariant Tori in the Restricted Three-body Problem," *20th AAS/AIAA Space Flight Mechanics Meeting*, San Diego, California, Feb. 2010.

[17] B. P. McCarthy, "Characterization of Quasi-Periodic Orbits for Applications in the Sun-Earth and Earth-Moon Systems," MS Thesis, Purdue University, West Lafayette, Indiana, Dec. 2018.

[18] N. Bosanac, "Bounded Motions Near Resonant Orbits in the Earth-Moon and Sun-Earth Systems," *AAS/AIAA Astrodynamics Specialist Conference*, Snowbird, Utah, Aug. 2018.

[19] N. Baresi and D. J. Scheeres, "Quasi-Periodic Invariant Tori of Time-Periodic Dynamical Systems: Applications to Small Body Exploration," *International Astronautical Congress*, Guadalajara, Mexico, Sept. 2016.

[20] A. Jorba, "Numerical Computation of the Normal Behavior of Invariant Curves of n-Dimensional Maps," *Nonlinearity*, Vol. 14, Sept. 2001, pp. 943–976.

[21] B. A. Steves, A. J. Maciejewski, and M. Hendry, eds., *Chaotic Worlds: From Order to Disorder in Gravitational N-Body Dynamical Systems*, Vol. II. Mathematics, Physics, and Chemistry - Vol 227 of *NATO Science*. Springer, 2006.

[22] C. H. Action, *Ancillary Data Services of NASA's Navigation and Ancillary Information Facility*, Jan. 1996. https://naif.jpl.nasa.gov/naif/.

[23] R. A. Bate, D. D. Mueller, and J. E. White, *Fundamentals of Astrodynamics*. Mineola, New York: Dover Publications, Inc, 1971.

[24] M. Vaquero and K. C. Howell, "Leveraging Resonant-Orbit Manifolds to Design Transfers Between Libration-Point Orbits," *Journal of Guidance, Control, and Dynamics*, Vol. 37, July 2014, pp. 1143–1157.

[25] M. T. Ozimek and K. C. Howell, "Low-Thrust Transfers in the Earth-Moon System, Including Applications to Libration Point Orbits," *Journal of Guidance, Control, and Dynamics*, Vol. 33, Apr. 2010, pp. 533–549.

[26] L. A. Hilday-Johnston and K. C. Howell, "Impulsive Time-Free Transfers Between Halo Orbits," *Celestial Mechanics and Dynamical Astronomy*, Vol. 64, May 1996, pp. 281–303.

[27] A. Haapala and K. C. Howell, "A Framework for Construction of Transfers Linking Periodic Libration Point Orbits in the Earth-Moon Spatial Circular Restricted Three-Body Problem," *Journal of Bifurcations and Chaos*, Vol. 26, May 2016, pp. 1630013–1–1630013–40.

[28] L. R. Capdevila and K. C. Howell, "Transfer Network Linking Earth, Moon, and the Triangular Libration Point Regions in the Earth-Moon System," *Advances in Space Research*, Vol. 62, Oct. 2018, pp. 1826–1852.

[29] R. E. Pritchett, E. M. Zimovan, and K. C. Howell, "Impulsive and Low-Thrust Transfer Design between Stable and Nearly Stable Periodic Orbits in the Restricted Problem," *18th AIAA SciTech Forum*, Kissimmee, Florida, Jan. 2018.

[30] A. Das-Stuart, K. C. Howell, and D. Folta, "Rapid Trajectory Design in Complex Environments Enable via Supervised and Reinforcement Learning Strategies," *69th International Astronautical Congress*, Bremen, Germany, Oct. 2018.

[31] D. C. Davis, S. M. Phillips, K. C. Howell, S. Vutukuri, and B. P. McCarthy, "Stationkeeping and Transfer Trajectory Design for Spacecraft in Cislunar Space," *AAS/AIAA Astrodynamics Specialist Conference*, Stevenson, Washington, Aug. 2017.

[32] R. Whitley and R. Martinez, "Options for Staging Orbits in Cislunar Space," *IEEE Aerospace 2015*, Big Sky, Montana, Mar. 2015.

[33] R. J. Whitley, D. C. Davis, L. M. Burke, B. P. McCarthy, R. J. Power, M. J. McGuire, and K. C. Howell, "Earth-Moon Near Rectilinear Halo and Butterfly Orbits for Lunar Surface Exploration," *AAS/AIAA Astrodynamics Specialist Conference*, Snowbird, Utah, Aug. 2018.

[34] C. E. Roberts, "Long Term Missions at the Sun-Earth Libration Point L1: ACE, WIND, and SOHO," *AAS/AIAA Astrodynamics Specialist Conference*, Girdwood, Alaska, Aug. 2011.

[35] W. H. Yu and K. Richon, "Launch Window Trade Analysis for the James Webb Space Telescope," *24th International Symposium on Space Flight Dynamics*, Laurel, Maryland, May 2014.

[36] N. Bosanac, C. M. Webster, K. C. Howell, and D. C. Folta, "Trajectory Design and Station-Keeping Analysis for the Wide Field Infrared Survey Telescope Mission," *AAS/AIAA Astrodynamics Specialist Conference*, Stevenson, Washington, Aug. 2017.